

Multi-loss ensemble deep learning for chest X-ray classification

Sivaramakrishnan Rajaraman^{1*}, Ghada Zamzmi¹, Sameer K. Antani¹

¹ National Library of Medicine, National Institutes of Health, Bethesda, MD, USA

* E-mail: sivaramakrishnan.rajaraman@nih.gov

Abstract

Medical images commonly exhibit multiple abnormalities. Predicting them requires multi-class classifiers whose training and desired reliable performance can be affected by a combination of factors, such as, dataset size, data source, distribution, and the loss function used to train the deep neural networks. Currently, the cross-entropy loss remains the de-facto loss function for training deep learning classifiers. This loss function, however, asserts equal learning from all classes, leading to a bias toward the majority class. In this work, we benchmark various state-of-the-art loss functions that are suitable for multi-class classification, critically analyze model performance, and propose improved loss functions. We select a pediatric chest X-ray (CXR) dataset that includes images with no abnormality (normal), and those exhibiting manifestations consistent with bacterial and viral pneumonia. We construct prediction-level and model-level ensembles, respectively, to improve classification performance. Our results show that compared to the individual models and the state-of-the-art literature, the weighted averaging of the predictions for top-3 and top-5 model-level ensembles delivered significantly superior classification performance ($p < 0.05$) in terms of MCC (0.9068, 95% confidence interval (0.8839, 0.9297)) metric. Finally, we performed localization studies to interpret model behaviors to visualize and confirm that the individual models and ensembles learned meaningful features and highlighted disease manifestations.

1. Introduction

Deep learning (DL) has demonstrated superior performance in natural and medical computer vision tasks. These include semantic segmentation, region of interest (ROI) detection, and classification, among others [1]. Computer-aided diagnostic tools developed with DL models have been widely used in analyzing medical images. Chest X-rays (CXRs) have been studied extensively where the models are used to predict manifestations of cardiopulmonary diseases such as pneumonia opacities, pneumothorax, cardiomegaly, Tuberculosis (TB), lung nodules, and, more recently, COVID-19 [2, 3]. Such tools are extremely helpful, particularly in resource-constrained regions where there exists a scarcity of expert radiologists.

1.1. Loss functions for model training

In supervised learning, the model parameters are iteratively modified to minimize the training error using several optimization methods (e.g., stochastic gradient descent). The error is computed using the loss function, also called a cost function, that maps model predictions to their associated costs. Cross-entropy loss is the commonly used loss function used for medical image classification tasks, including CXRs [4 – 8]. This loss function outputs a class probability value between 0 and 1, where high values indicate high disagreement of the predicted class with the ground truth label. In class-imbalanced medical image classification tasks, training a model to minimize the cross-entropy loss might lead to biased learning since (i) the loss asserts equal weights to all the classes, and (ii) the model would predict the majority of test samples as belonging to the dominant normal class. In this regard, the authors of [9] proposed a loss function, called focal loss, for object detection tasks. Here, the standard cross-entropy loss function is modified to down weight the majority background class so the model would focus on learning the minority object samples. Following this study, focal loss function has been used in several medical image classification studies. For example, the authors of [10] trained DL models to minimize focal loss and improve pulmonary nodule detection and classification performance using computed tomography (CT) scans. They observed that the model trained with focal loss resulted in superior performance with 97.2% accuracy and 96.0% sensitivity. Another study [11] used focal loss to train the models toward classifying CXRs into normal, bacterial pneumonia, viral pneumonia, or COVID-19 categories. It was observed that the models trained with focal loss outperformed other models by demonstrating superior values for precision (78.33%), recall (86.09%), and F-score (81.68%). Aside from these studies, the literature does not have a comprehensive study that investigates the effects of loss functions on medical image classification, particularly CXRs.

1.2. Modality-specific knowledge transfer

DL models, unlike conventional machine learning models, require a huge amount of labeled data to learn meaningful features and categorize images into their respective categories. The need for relatively large datasets introduces a major challenge in medical image classification tasks since there is a significant scarcity of labeled data. Under these circumstances, DL models are often pretrained on a large selection of natural images such as ImageNet [12]. These models are then used to transfer knowledge to improve performance in another task, i.e., the target task. This approach, known as transfer learning, is widely adopted in natural and medical computer vision tasks due to the lack of large image datasets. However, medical images have unique visual characteristics such as color distribution, texture, object contours, and

orientation [1]. Therefore, transferring the knowledge from a model trained on natural images may not be ideal for reliable, repeatable, and robust disease classification.

CXRs have been extensively studied in DL-based disease prediction and also, we have many radiologists-verified and clinically proven datasets available for study [4 – 7]. These datasets can be used to train DL models and transfer CXR modality-specific knowledge to a relevant target task. A study of the literature shows several methods for retraining the ImageNet-pretrained models using a large collection of CXR images to update the weights, specific to the CXR image modality. This helps the models to learn meaningful modality-specific features that are relevant to be transferred to improve performance in another CXR classification task. In another study [3], the authors performed CXR modality-specific pretraining using a combined selection of publicly available CXR collections. The lungs are segmented to help models learn meaningful feature representations and identify normal and abnormal lungs. The learned knowledge is transferred to improve performance in classifying another collection of CXRs as showing COVID-19 manifestations, or normal lungs. The authors of [13] performed CXR modality-specific pretraining of the SOTA DL models using the NIH-CXR [4] dataset. The learned knowledge was transferred to improve performance in a TB classification task. Similarly, the authors of [14] retrained the models on the RSNA CXR [5] collection and transferred the CXR modality-specific knowledge to classify CXRs in another collection as showing normal lungs or COVID-19 manifestations. The authors of [15] used the CheXpert [6] CXR dataset to retrain ImageNet-trained models and update the weights specific to the CXR image modality. The learned knowledge was transferred to improve performance in classifying CXRs as showing normal or abnormal lungs. In another study [16], the authors retrained the ImageNet-pretrained models on a combined collection of RSNA, pediatric pneumonia [7], and Indiana [17] CXR collections to learn the characteristics of normal and abnormal lungs. The learned knowledge was transferred to improve performance toward a relevant task of classifying CXRs as showing normal lungs or TB-like manifestations. The authors of [18] proposed a multi-task training methodology using CXR modality-specific pretrained models to improve performance toward classifying CXRs into normal or abnormal categories. The authors observed that the accuracy increased by 6% (86% accuracy) with CXR modality-specific knowledge transfer compared to the 80% accuracy achieved with ImageNet-pretrained models. These studies reveal that CXR modality-specific knowledge transfer improved classification performance in relevant CXR classification tasks.

1.3. Ensemble deep learning

DL models learn a mapping function through error backpropagation and update model weights to minimize error. They can vary in their architecture, hyper-parameters, and training strategy, thereby resulting in varying degrees of bias and variance errors. Bias provides a measure of variation in the model's

prediction from the desired target value during training. The variance measure provides the change in the model’s performance with different fragments of the training dataset. Ensemble models help (i) reduce prediction variance and achieve improved performance over any individual constituent model, and (ii) increase robustness by reducing the range (spread) of the predictions. There are several ensemble methods reported in the literature including majority voting, simple averaging, weighted averaging, and stacking, among others [19].

Ensemble models have been widely used in medical image classification tasks including CXRs. For example, the authors of [8] performed ensemble learning to classify CXRs showing TB manifestations. They used an ensemble of AlexNet and GoogLeNet models to achieve a 0.99 area under the receiver operating characteristic curve (AUROC or AUC). In another study [3], the authors constructed ensembles of state-of-the-art (SOTA) DL models that were pretrained with CXRs to construct CXR modality-specific pretrained models. These were used to classify CXRs in another collection into normal or COVID-19 classes. The authors observed that the weighted averaging ensemble of the top-3 performing models improved classification and ROI localization performance with an accuracy of 90.97% and AUC of 0.9508 as compared to any of the individual constituent models. In [13], the authors discussed the benefits of training CXR modality-specific model ensembles toward classifying CXRs into normal or TB categories and demonstrated 94.89% accuracy. Other ensemble-based methods for CXR classification can be found in [14 – 16, 20 – 24]. Also, these studies trained ensemble models to minimize the de-facto cross-entropy loss in their respective classification tasks. We observed that no studies report evaluations on the performance of ensemble DL models trained with other loss functions toward improving classification performance.

1.4. Statistical analysis

Statistical analysis is indispensable in scientific studies as it helps avoid (i) evaluation biases due to the dataset used, (ii) inappropriate mining of data during training, and (iii) any other assumption violations. In this study, we analyze the relationship observed between the input and output variables and report statistical significance in the results. We measure the binomial confidence intervals (CIs) as the exact Clopper–Pearson interval for the MCC metric to analyze statistical significance.

1.5. Rationale of the study

We study the combined benefits of (i) transferring knowledge from a CXR modality-specific pretrained model that is trained using the existing and proposed loss functions and (ii) constructing ensembles using models from step (i) to improve performance in a multi-class classification task that

classifies pediatric CXRs as showing normal lungs, bacterial pneumonia, or viral pneumonia manifestations. This systematic study is performed as follows. First, we train an EfficientNet-B0-based U-Net model on a collection of CXRs and their associated lung masks [25] to segment lungs in the pediatric pneumonia CXR collection [7]. We select the EfficientNet-B0-based model because it delivered SOTA performance in ImageNet classification tasks with reduced computational complexity [26]. Next, the encoder from the trained EfficientNet-B0-based U-Net model is truncated and appended with classification layers. This is done to transfer CXR modality-specific knowledge for improving performance in the task of classifying CXRs in the pediatric pneumonia CXR dataset into normal, bacterial pneumonia, or viral pneumonia categories. Finally, the top-K ($K = 3, 5$) performing models are used to construct prediction-level and model-level ensembles. At the prediction level, the ensembles are constructed with majority voting, simple averaging, weighted averaging, and stacking methods using the models' predictions. At the model level, the top-K models are instantiated with their trained weights and truncated at their deepest convolutional layer. The feature maps from these layers are concatenated and appended with a 1×1 convolutional layer to reduce feature dimensions. This is followed by appending classification layers to predict CXRs into their respective categories. The performance of the individual models, prediction-level, and model-level ensembles are further analyzed for statistical significance. We also performed localization studies to visualize and ensure that the individual models and their ensembles learned meaningful features and highlighted the disease-manifested ROIs in the CXRs.

The rest of the manuscript is organized as follows: Section 2 discusses the materials and methods, Section 3 describes the results and Section 4 discusses the results, limitations, and concludes the study.

2. Materials and Methods

2.1. Datasets

This retrospective study uses the following two datasets:

- (i) Montgomery TB CXRs [27]: This is a publicly available collection of 58 CXRs showing TB-related manifestations and radiologist readings and 80 CXRs showing lungs with no findings. The images and their associated lung masks are deidentified and exempted from the National Institutes of Health (NIH) IRB review (OHSRP#5357). We use this as an independent test set to evaluate the segmentation model proposed in this study.
- (ii) Pediatric pneumonia [7]: A set of 4273 CXRs showing lungs infected with bacterial and viral pneumonia and 1583 CXRs showing normal lungs are collected from children of 1 to 5 years of age at the Guangzhou Medical Center in China. The author-defined [7] training set contains 1349, 2538, and 1345 CXRs and the test set contains 234, 242, and 148 CXRs showing normal lungs, bacterial

pneumonia, and viral pneumonia manifestations, respectively. The CXRs are acquired as a part of routine clinical care, curated by expert radiologists, and made publicly available with IRB approvals. We use this dataset toward classifying CXRs as showing normal lungs, bacterial pneumonia, or viral pneumonia manifestations.

2.2. Lung Segmentation and Cropping

As CXR images contain irrelevant regions that do not help in learning meaningful features, we segmented the ROI, i.e., the lungs from the CXRs, and used the lung-segmented images for model training. Literature studies reveal that U-Net [28] is widely used for segmenting the ROIs in natural and medical images. Further, the study of the literature shows that EfficientNet [26] models have achieved superior performance in natural and medical computer vision tasks, as compared to other models, in terms of accuracy, efficiency, and computational complexity. Hence, we used an EfficientNet-B0-based U-Net model [29] to perform pixel-wise segmentation.

2.2.1. Segmentation losses

The segmentation model is trained to minimize the following loss functions: (i) Binary cross-entropy (BCE), (ii) Weighted BCE-Dice, (iii) Focal, (iv) Tversky, and (v) Focal Tversky. The BCE loss is the de-facto loss function used in image segmentation tasks. The BCE loss provides a measure of disagreement between the ground truth and predictions for a set of events. It is defined as,

$$BCE\ loss = -(y\log(p) + (1 - y)\log(1 - p)) \quad (1)$$

$$BCE\ loss = \{-\log(p),\ when\ y = 1, -\log(1 - p),\ otherwise \quad (2)$$

Here, y is the actual value, and p is the predicted value. The value of $y \in \{0,1\}$ denotes the target class label and $p \in [0,1]$ denotes the estimated probability of the model when $y=1$. The above equation can be rewritten in simplistic terms as,

$$p_t = \{p,\ when\ y = 1; (1 - p),\ otherwise \quad (3)$$

$$BCE(y, p) = BCE(p_t) = -\log(p_t) \quad (4)$$

Dice loss is another widely used loss function in image segmentation tasks [30]. The Dice loss is given by,

$$Dice\ loss\ (y, p) = 1 - \frac{2yp + 1}{y + p + 1} \quad (5)$$

The authors of [3] demonstrated that a weighted combination of BCE loss and Dice loss delivered superior ROI segmentation performance using CXRs. Hence, we used a weighted combination of these losses as given by,

$$\text{Weighted Loss}_{\text{BCE-Dice}} = \alpha \cdot \text{BCE loss}_m + \beta \cdot \text{Dice loss}_m \quad (6)$$

Here, α and β are the weights and m is the batch number. The losses are computed and updated for every mini-batch and the final loss is computed as the mean of the losses across the mini-batches. The values of α and β are determined empirically to be 0.5.

The principal limitation of BCE loss is that it asserts equal learning from all image pixels. This adversely impacts segmentation performance in case of an imbalanced number of background and ROI pixels. This is especially true for medical images, particularly CXRs, where the ROI constituting the lungs, contributes a smaller portion of the entire image. Under these circumstances, the authors of [13] proposed the focal loss to down weight the majority background and focus on learning minority ROI class pixels. The focal loss is given by,

$$\text{Focal loss}(p_t) = -\alpha_t(1 - p_t)^\gamma \log(p_t) \quad (7)$$

Here, γ denotes the focusing parameter that determines the rate at which the majority class samples are down-weighted. When $\gamma = 0$, the equation converges to BCE loss. In this study, the value of γ is set empirically to 1.

Tversky loss, which was proposed in [31], provides a superior tradeoff between precision and recall for class-imbalanced segmentation tasks. It is given by,

$$\text{Tversky Loss}_c(a, b) = \frac{\sum_{m=1}^M x_{0m}y_{0m}}{\sum_{m=1}^M x_{0m}y_{0m} + a \sum_{m=1}^M x_{0m}y_{1m} + b \sum_{m=1}^M x_{1m}y_{0m}} \quad (8)$$

Here, c denotes the classes, 0 for the lung ROI, and 1 for the background. The values a and b denote hyperparameters of the Tversky loss function. The x and y values denote predicted and target labels, respectively. The value x_{0m} denotes the probability of a pixel m to belong to class 0, i.e., lung ROI while x_{1m} denotes the probability of the pixel to belong to class 1, i.e., the background, $y_{0m} = 1$ for every lung pixel and 0 for the background, $y_{1m} = 1$ for every background pixel and 0 for the lung pixel. It has been demonstrated by the authors of [31] that higher values of a resulted in improved convergence, generalization and minimized the number of false negatives (FN). After empirical evaluations, we set the value of $a = 0.7$ and $b = 0.3$.

A variant of the Tversky loss, called Focal Tversky loss, was proposed by [32]. This loss is given by,

$$\text{Focal Tversky Loss}_c = \sum_{c=0,1} (1 - TL_c)^{1/\gamma} \quad (9)$$

The value of γ is set to 4/3 as suggested in [32].

The EfficientNet-B0-based U-Net model is trained using the CXR collection and their associated lung masks discussed in [25] to minimize BCE, weighted BCE-Dice, focal, Tversky, and focal Tversky loss functions. We allocated 10% of the training data for validation with a fixed seed. Each mini-batch of the

data is augmented using random affine transformations such as pixel shifting [-2 +2], horizontal flipping, and rotations [-5 +5] to introduce variability into the training process. The model is trained using an Adam optimizer with an initial learning rate of 0.001. Model checkpoints are stored after each epoch. The learning rate is reduced whenever the validation loss plateaued. The model demonstrating the least validation loss is used to predict lung masks of a reduced 512×512 pixel resolution for the CXRs in the Montgomery TB CXR collection. The images are resized using bicubic interpolation from OpenCV software libraries. An evaluation against a cross-institutional dataset such as the Montgomery CXR dataset provides a faithful measure of segmentation performance.

2.2.2. Segmentation evaluation metrics

The performance of the individual models is evaluated using the following metrics: (i) Segmentation accuracy; (ii) Dice coefficient, and (iii) Intersection over union (IoU). The segmentation accuracy is given by,

$$Accuracy = \frac{(TP + TN)}{(TP + TN + FP + FN)} \quad (10)$$

Here, TP denotes the number of true positives, i.e., pixels classified correctly as belonging to the lung ROI, TN denotes the number of true negatives, i.e., pixels classified correctly as belonging to the background, FP denotes the number of false positives, i.e., pixels classified incorrectly as belonging to the lung ROI, and FN denotes to the number of false negatives, i.e., pixels classified incorrectly as belonging to the background.

Dice coefficient provides a measure of similarity between the images. It is given by,

$$Dice\ coefficient = \frac{2 \times TP}{(TP + FP) + (TP + FN)} \quad (11)$$

The value of the Dice coefficient ranges from 0 to 1, where 0 denotes no similarity and 1 denotes a complete similarity.

The IoU metric is another widely used metric to evaluate segmentation performance. It provides a measure of the intersection and union between the target and predicted masks and is given by,

$$IoU = \frac{TP}{(TP + FP + FN)} \quad (12)$$

The segmentation accuracy provides a biased estimate if the background takes a larger portion of the image as compared to the ROI. Under these circumstances, the IoU metric would help evaluate segmentation performance by (i) computing the IoU for the ROI and background classes separately and (ii) averaging over both the classes to provide a global score.

2.2.3. Segmentation model ensemble

We selected the top-3 models from those that are trained using the aforementioned loss functions based on accuracy, IoU, and Dice coefficient metrics. The selected models are used to predict the lung masks for the CXRs in the Montgomery CXR collection. These masks are then bitwise-ANDed to produce the final lung mask. The bitwise-AND operation compares each pixel of the predicted masks by the top-3 performing models. If only all the pixels are 1, i.e., belonging to the lung ROI, the corresponding bit in the final mask is set to 1, otherwise, it is set to 0. The final lung mask is then overlaid on the original CXR image to delineate the lung boundaries and the bounding box containing the lung pixels is cropped. The resulting lung-cropped image is resized to 512×512 pixel resolution. Then, the cropped CXRs are contrast-enhanced by saturating the top and bottom 1% of all the image pixels followed by normalizing the pixels to the range $[0, 1]$. Fig 1 shows the diagram of the segmentation module proposed in this study.

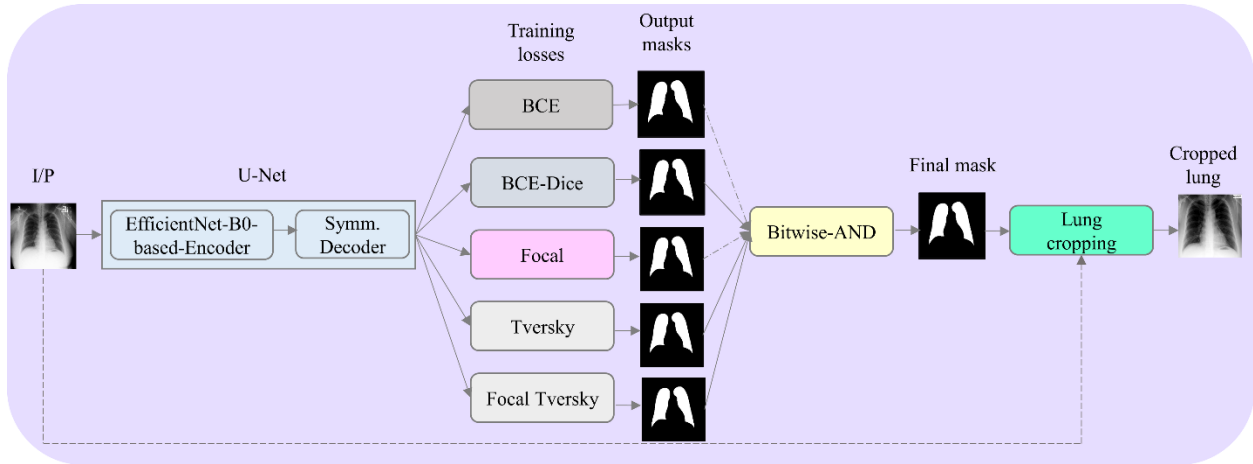


Fig 1. Segmentation module. The U-Net constructed with an EfficientNet-B0-based encoder and symmetrical decoder [29] is trained to minimize the following losses: (i) BCE; (ii) Weighted BCE-Dice, (iii) Focal, (iv) Tversky, and (v) Focal Tversky. The trained models predict lung masks in the Montgomery TB CXR collection. The predictions of the top-3 performing models are bitwise-ANDed to produce the final lung mask.

2.3. Classification module

The encoder from the trained EfficientNet-B0-based U-Net model is truncated at the ‘block5c_add’ layer (TensorFlow Keras naming convention) with feature map dimensions of $[16, 16, 512]$. This approach is followed to transfer CXR modality-specific knowledge to improve performance in the current CXR classification task. The truncated model is appended with the following layers: (i) a zero-padding (ZP) layer, (ii) a convolutional layer with 512 filters, each of size 3×3 , (iii) a global averaging pooling (GAP)

layer; and (iv) a final dense layer with three neurons and Softmax activation, to classify the pediatric CXRs as showing normal lungs, bacterial pneumonia, or viral pneumonia manifestations.

We used the train and test splits published in [7] to compare our model performance with the SOTA literature [7], [33]. We allocated 10% of the training data for validation with a fixed seed. The model is trained using a stochastic gradient descent optimizer with an initial learning rate of 0.001 and momentum of 0.9, to minimize the loss functions discussed in Sections 2.3.1.1 and 2.3.1.2. We used checkpoints to store the model weights after each mini-batch update. The best-performing model is selected based on the least loss obtained with the validation data. These models are evaluated with the test set, and the performance is recorded in terms of the following metrics: (a) accuracy; (b) AUROC; (c) area under the precision-recall curve (AUPRC); (d) precision; (e) recall; (f) F-score; and (g) MCC.

The top-K ($K=3, 5$) models that deliver superior performance with the test set are used to construct the ensembles. We constructed prediction-level and model-level ensembles. At the prediction level, the models' predictions are combined using various ensemble strategies such as majority voting, simple averaging, weighted averaging, and stacking. In a majority voting ensemble, the most voted predictions are considered final for classifying CXRs to their respective classes. In a simple averaging ensemble, the individual model predictions are averaged to generate the final prediction. For the weighted averaging ensemble, we propose to optimize the weights that minimize the total logarithmic loss so that the predicted labels converge to the target labels. We iteratively minimized the logarithmic loss using the Sequential Least-Squares Programming (SLSQP) algorithm [34]. In a stacking ensemble, the predictions are fed into a meta-learner that consists of a single hidden layer with 9 and 15 neurons respectively, for the top-3 and top-5 performing models. The weights of the top-K models are frozen and only the meta-learner is trained to optimally combine the models' predictions. A dense layer with three neurons and Softmax activation is appended to output prediction probabilities. Fig 2 shows the classification and ensemble frameworks proposed in this study.

For the model level ensemble, the top-K models are instantiated with their trained weights and truncated at their deepest convolutional layer. The features from these layers are concatenated and appended with a 1×1 convolutional layer, to reduce feature dimensions. This is followed by appending a GAP layer and a dense layer with three neurons and Softmax activation to classify the CXRs as showing normal lungs, bacterial pneumonia, or viral pneumonia manifestations. The performance of the individual models, prediction-level ensembles, and model-level ensembles are further compared for statistical significance. All the models are trained and evaluated using Tensorflow Keras 2.4 on a Windows system with an Intel Xeon 3.80 GHz CPU, NVIDIA GeForce GTX 1050 Ti GPU, and CUDA dependencies for GPU acceleration.

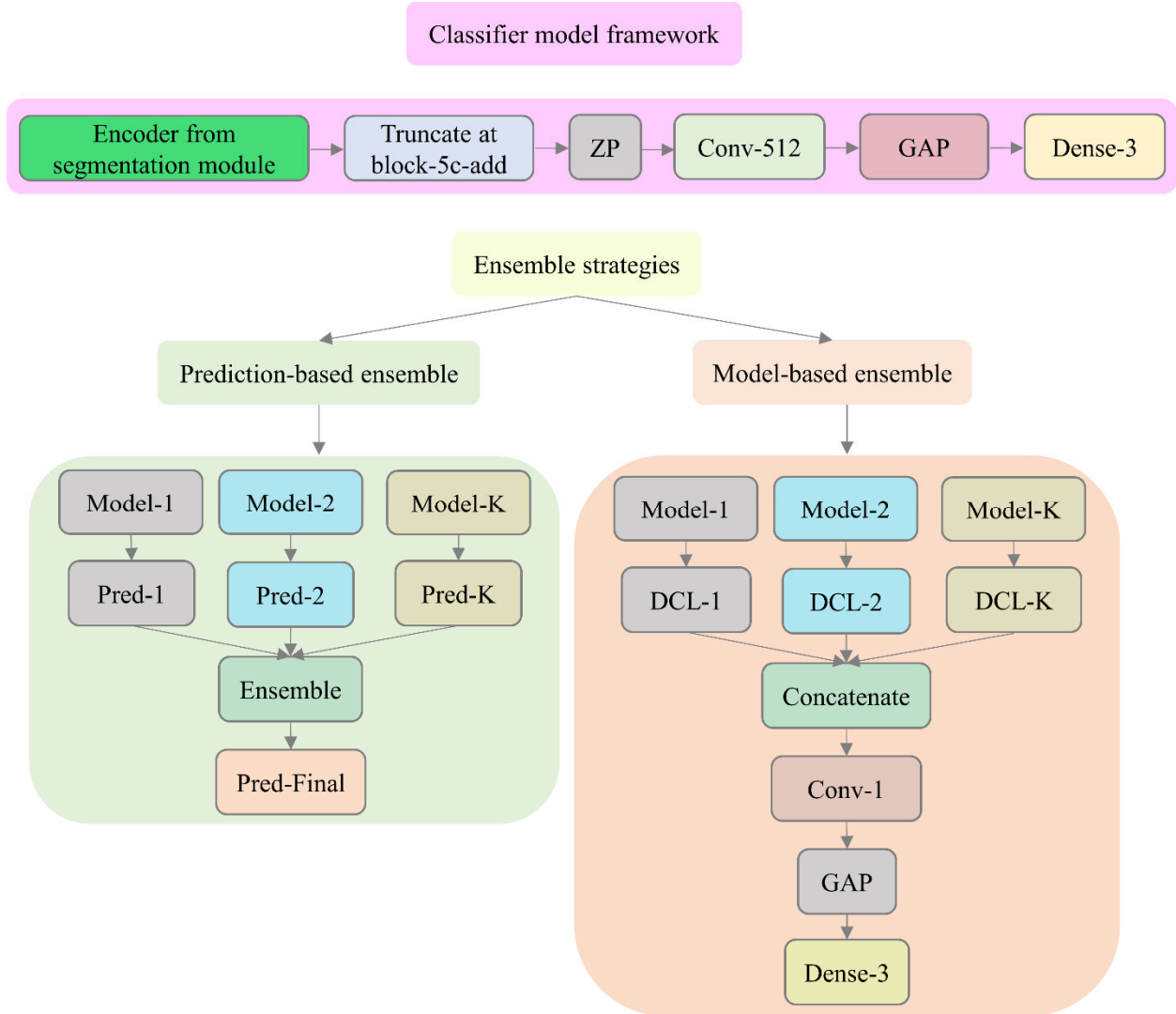


Fig 2. Classification module. The EfficientNet-B0-based encoder is truncated at the block-5c-add layer and appended with the classification layers to output multi-class prediction probabilities. GAP denotes the global average pooling layer and DCL denotes the deepest convolutional layer in the trained models. The classification model is trained to minimize the various loss functions discussed in Section 2.3.1.1 and Section 2.3.1.2. The top-K ($K = 3, 5$) performing models are used to construct prediction-level and model-level ensembles.

2.3.1. Classification losses:

2.3.1.1. Existing classification loss functions:

We used several existing loss functions as follows for the multi-class classification task under study: (i) Categorical cross-entropy (CCE) loss; (ii) Categorical focal loss; (iii) Kullback-Leibler (KL) divergence loss; (iv) Categorical Hinge loss; (v) Label-smoothed CCE loss; (vi) Label-smoothed categorical focal loss, and (vii) Calibrated CCE loss [35]. We discuss these losses as shown below.

(i) Categorical cross-entropy (CCE) loss:

The CCE loss provides a measure of disagreement between the actual target and predictions. It is the de-facto loss function used in multi-class classification problems. The CCE loss is given by,

$$CCE\ loss = - \sum_{k=1}^{output\ size} y_k \cdot \log (y'_k) \quad (13)$$

Here, y'_k denotes the k^{th} scalar value in the model output, y_k denotes the corresponding target value, and the *output size* denotes the number of scalar values in the model output. The value of y_k denotes the probability that the event k occurs and the sum of all y_k is 1 that infers that exactly one event may occur. The negative sign ensures that the loss gets minimized with an increasing agreement between the target and predicted distributions.

(ii) Categorical focal loss:

The principal limitation of CCE loss is that the loss asserts equal learning from all the classes. This adversely impacts training and classification performance during class-imbalanced training. This holds for medical images, particularly CXRs, where a class imbalance exists between the majority normal class and other minority disease classes. In this regard, the authors of [9] proposed the focal loss for object detection tasks, in which the standard cross-entropy loss function is modified to down weight the majority class so that the model would focus on learning the minority classes. In a multi-class classification setting, the categorical focal loss is given by,

$$Categorical\ Focal\ loss\ (L(k, p)) = -(1 - p'_k)^\gamma \log (p'_k) \quad (14)$$

Here, $K = 3$, denotes the number of classes, $k = \{0, 1, K - 1\}$ denotes the class labels for bacterial pneumonia, normal, and viral pneumonia classes respectively, and $p = (p'_0, p'_1, p'_2) \in [0, 1]^3$ is a vector representing an estimated probability distribution over the three classes. The value γ denotes the rate at which the easy samples are down-weighted. The categorical focal loss converges to CCE loss at $\gamma = 0$. Through empirical evaluation, we set the value of $\gamma = 1$ in this study.

(iii) Kullback-Leibler (KL) divergence loss:

The KL divergence, also called relative entropy, measures the difference between the observed and actual probability distributions. The KL divergence between two distributions $A(x)$ and $B(x)$ is given by,

$$KL\ divergence(A||B) = \sum_{x \in X} A(x) \log \left(\frac{A(x)}{B(x)} \right) \quad (15)$$

Notably, the KL divergence measure is asymmetrical and is given by,

$$KL\ Divergence(A||B) \neq KL\ Divergence(B||A) \quad (16)$$

This infers that the KL divergence value will be large if the probability for an event in A is large and the probability for the same event in B is small. However, the divergence will be still large, but may not be as large as in the first case, when the probability from A is small and the probability from B is large.

(iv) Categorical Hinge loss:

The Hinge loss is widely used in binary classification problems to produce “maximum-margin” classification [36], particularly with SVM classifiers. This loss could be used in a multi-class classification setting and is given by,

$$\text{Categorical Hinge loss} = \text{Max}(\text{negative} - \text{positive} + 1, 0) \quad (17)$$

$$\text{negative} = \text{Max}((1 - y_{\text{true}}) * y_{\text{pred}}) \quad (18)$$

$$\text{positive} = \text{Sum}(y_{\text{true}} * y_{\text{pred}}) \quad (19)$$

Here, y_{true} and y_{pred} denote the ground truth one-hot encoded labels and predictions, respectively.

(v) Label smoothed CCE and categorical focal losses:

DL models are prone to become overconfident; hence, they may overfit the training data. Although several regularization methods have been proposed to tackle overfitting issues, only a few strategies have been effectively proposed to combat overconfidence. Label smoothing [37] is a regularization technique that helps to address both overfitting and overconfidence issues. Label smoothing alleviates overconfidence issues by replacing the one-hot encoded label vector $y_{\text{one-hot-encoded}}$ with a mixture of $y_{\text{one-hot-encoded}}$ and uniform distribution. This can be expressed as,

$$y_{\text{label-smooth}} = (1 - \sigma) * y_{\text{one-hot-encoded}} + \sigma/C \quad (20)$$

Here, σ denotes the smoothing parameter, $y_{\text{one-hot-encoded}}$ denotes the one-hot encoded labels, and $C = 3$ denotes the number of classes. The value of $\sigma = 0$ gives the original one-hot encoded labels, and $\sigma = 1$ gives a uniform distribution. We applied label smoothing to the CCE and categorical focal losses. We tested different weights for $\sigma = [0.1, 0.2, 0.3, 0.4]$. Through empirical evaluations, the value of $\sigma = 0.2$ improved performance for the CCE and categorical focal losses.

(vi) Calibrated CCE loss:

The prediction probabilities should reflect the true occurrence likelihood of the events. However, DL models may produce overconfident predictions, particularly during class-imbalanced training [38]. The models may overfit and are said to be poorly calibrated. Therefore, a linear relationship fails to exist between the accuracy and the predicted probabilities. To alleviate these issues, the authors of [35] proposed to add the difference between the accuracy and predicted probabilities as an auxiliary term to the CCE loss.

This serves as a regularization parameter that penalizes the model when there is a reduction in the CCE loss, but the accuracy plateaued. This modified loss is called the calibrated CCE loss and is given by,

$$\text{Calibrated CCE loss} = -1/K \sum_{k=1}^K (y_k \cdot \log p(y_k)) + \lambda \cdot \text{difference} \quad (21)$$

Here, $K = 3$ denotes the number of classes, y_k denotes the true label, and $p(y_k)$ denotes the predicted probability. The auxiliary term *difference* is calculated for each mini-batch, as given by,

$$\text{difference} = |1/K \sum_{k=1}^K c_k - 1/K \sum_{k=1}^K p(y'_k)| \quad (22)$$

Here, y'_k denotes the predicted label. The value of c_k is 1 if $y'_k = y_k$; otherwise, c_k is 0. This auxiliary term forces the average value of the predicted probabilities to match the accuracy over all training examples. This pushes the model closer to the ideal situation, where the model accuracy would reflect the true occurrence likelihood of the samples. The auxiliary term serves as a smoothing parameter for predictions with extremely low or high prediction confidences. We tested with different weights for $\lambda = [0.5, 1, 2, 5, 10, 15, 20]$. After empirical evaluations, the value of λ is set to 10.

2.3.1.2. Proposed loss functions:

We propose the following loss functions for the current task of classifying CXRs into multiple classes as showing normal lungs, bacterial, or viral manifestations: (i) CCE loss with entropy-based regularization; (ii) Calibrated negative entropy loss, (iii) Calibrated KL divergence loss; (iv) Calibrated categorical focal loss, and (v) Calibrated categorical Hinge loss. The details of the proposed loss functions are discussed below.

(i) CCE with entropy-based regularization:

The DL models demonstrate low entropy values for the output distributions when they are confident about their predictions. However, under class-imbalanced training conditions, DL models may be overconfident about the majority class, and it may classify most of the samples as belonging to this dominant class. This may lead to model overfitting and adversely impact generalization performance. Under these circumstances, a penalty could be introduced in the form of a regularization term that penalizes peaked distributions, thereby reducing overfitting and improving generalization. A model produces a conditional distribution $p_{\Omega}(y|x)$ through the Softmax function, over a set of classes y given an input x . The entropy of this conditional distribution is given by,

$$H(p_{\Omega}(y|x)) = - \sum_k p_{\Omega}(y_k|x) \log(p_{\Omega}(y_k|x)) \quad (23)$$

Here, H denotes the entropy term. A regularization term is proposed where the negative entropy is added to the negative log-likelihood to penalize over-confident output distributions. It is given by,

$$entropy - reg(\Omega) = - \sum \log p_{\Omega}(y|x) - \beta H(p_{\Omega}(y|x)) \quad (24)$$

Here, β controls the intensity of the penalty. Through empirical evaluations, we set the value of $\beta = 2$. We used this regularization term in the final dense layer as an activity regularizer and trained the model to minimize the CCE loss.

(ii) Calibrated negative entropy loss:

We propose an entropy-based loss function where the negative entropy is added as an auxiliary term to the negative log-likelihood term as shown in equations [23] and [24] to penalize over-confident output distributions. A model is said to demonstrate poor calibration if it is overconfident or underconfident about its predictions and would not reflect the true occurrence likelihood of the class events. Motivated by [35], we propose to add a regularization term that computes the difference between the accuracy and the predicted probabilities to the entropy-based loss function. This regularization term helps to penalize the model when the entropy-based loss function reduces without a corresponding change in the accuracy. The regularization term forces the accuracy to match the average predicted probabilities, thereby (i) acting as a smoothing parameter that smoothens overconfident or underconfident predictions and (ii) pushing the model to converge to the ideal condition when the accuracy would reflect the true occurrence likelihood. The calibrated negative entropy loss is given by,

$$Calibrated\ negative\ entropy\ loss = - \sum \log p_{\Omega}(y|x) - \beta H(p_{\Omega}(y|x)) + \lambda \cdot difference \quad (25)$$

Here, β controls the penalty intensity. The auxiliary term *difference* is calculated for each mini-batch, as given in equation [22]. We tested with different weights for $\beta = [0.00001, 0.0001, 0.001, 0.01, 0.1, 1, 2]$ and $\lambda = [0.5, 1, 2, 5, 10, 15, 20]$. After empirical evaluations, we set the value of $\beta = 0.001$ and $\lambda = 10$.

(iii) Calibrated KL divergence loss:

We propose to benefit from the regularization term mentioned in equation [22] to smoothen model predictions when trained to minimize the KL divergence loss. We propose the calibrated KL divergence loss where the regularization term in equation [22] is added to the KL divergence loss. This is done to penalize the model when the KL divergence loss reduces without a corresponding change in the accuracy. The calibrated KL divergence loss is given by,

$$Calibrated\ KL\ divergence\ loss = KL\ Divergence(A||B) + \lambda \cdot difference \quad (26)$$

The auxiliary term *difference* is calculated for each mini-batch and is given by equation [22]. We tested with different weights for $\lambda = [0.5, 1, 2, 5, 10, 15, 20]$. After empirical evaluations, the value of λ is set to 1.

(iv) Calibrated categorical focal loss:

We propose the calibrated categorical focal loss, where the difference between the accuracy and predicted probabilities is added as a regularization term to penalize the model for overconfident and underconfident predictions when trained to minimize the categorical focal loss. The calibrated categorical focal loss is given by,

$$\text{Calibrated categorical focal loss} = -(1 - p'_y)^\gamma \log(p'_y) + \lambda \cdot \text{difference} \quad (27)$$

The auxiliary term *difference* is calculated for each mini-batch and is given by equation [22]. We tested with different weights for $\gamma = [0.5, 1, 2, 5]$ and $\lambda = [0.5, 1, 2, 5, 10, 15, 20]$. After empirical evaluations, the value of γ and λ is set to 1.

(v) Calibrated categorical Hinge loss:

We propose the calibrated categorical Hinge loss, where the difference between the accuracy and predicted probabilities is added as an auxiliary term to the categorical Hinge loss. This auxiliary term penalizes the model when the categorical Hinge loss reduces without a corresponding change in the accuracy. The calibrated categorical Hinge loss is given by,

$$\text{Calibrated categorical Hinge loss} = \text{Max}(\text{negative} - \text{positive} + 1, 0) + \lambda \cdot \text{difference} \quad (28)$$

The *negative* and *positive* terms are given by equations [18] and [19]. The auxiliary term *difference* is calculated for each mini-batch and is given by equation [22]. We tested with different weights for $\lambda = [0.5, 1, 2, 5, 10, 15, 20]$. After empirical evaluations, the value of λ is set to 10.

2.4. Model Interpretation Through Disease ROI Localization

A principal limitation of DL models is the inability to “explain” their learned behavior. This is attributed to (i) their architectural depth, thereby having a huge number of model parameters that prevent decomposing and explaining individual components, and (ii) the characteristics of the models to approximate non-linear functions, perform complex data transformations and make predictions that are divided by a non-linear decision boundary. The lack of explainability of DL models is considered a serious bottleneck in medical visual recognition tasks, where it is indispensable to provide meaningful clinical interpretations. Several approaches have been proposed in the literature to interpret the learned behavior of these models. For example, the authors of [39] proposed class-activation mapping (CAM)-based methods.

Here, the decision made by the DL models is interpreted by highlighting image pixels with varying intensities that contribute to the class predictions. This approach could be applied only to the models with a fixed architecture. A variant of CAM, called gradient-weight CAM (Grad-CAM) [40], was proposed to deal with models of varying architectures. Grad-CAM-based localization is extensively used in medical image classification tasks, particularly using CXRs [2], [3], [8], [14 – 16]. In this study, we used Grad-CAM tools to help interpret the learned behavior of the top-K performing models and their ensembles.

3. Results

In this section, we present the results of CXR lung segmentation (Section 2.2) and classification (Section 2.3).

3.1. CXR lung segmentation

Recall that an EfficientNet-B0-based U-Net model is trained to minimize BCE, weighted BCE-Dice, focal, Tversky, and focal Tversky loss functions and predict lung masks for the CXRs in the Montgomery TB CXR collection. The lung masks predicted by the top-3 performing models are bitwise-ANDed to produce the final lung mask. The performance of the individual models and the bitwise ANDed model ensemble is evaluated using segmentation accuracy, IoU, and Dice coefficient as shown in Table 1. Fig 3 shows the polar coordinates plot summarizing the segmentation performance.

Table 1. Segmentation performance achieved by the individual models and the bitwise-ANDed ensemble of the top-3 performing models. The bold numerical values denote the best performance in respective columns.

Loss/Method	Metrics		
	IoU	Dice	Accuracy
BCE	0.8186±0.0384	0.9571±0.0361	0.9720±0.0096
Weighted BCE-Dice	0.8465±0.0401	0.9601±0.0396	0.9732±0.0104
Focal	0.2601±0.0621	0.9189±0.0527	0.7788±0.0485
Tversky	0.9360±0.0368	0.9624±0.0225	0.9912±0.0102
Focal Tversky	0.9510±0.0415	0.9637±0.0271	0.9925±0.0130
Ensemble	0.9518±0.0462	0.9652±0.0309	0.9927±0.0117

From Fig 3, we observed that the segmentation model demonstrated higher values for the Dice coefficient compared to the IoU metrics due to the way the two functions are defined. The Dice coefficient value is given by twice the area of the intersection of two masks, divided by the sum of the areas of the masks. It is observed from Table 1 that, considering individual models, the segmentation model trained to minimize the focal Tversky loss demonstrated superior performance in terms of IoU, Dice coefficient, and

accuracy metrics, followed by those trained with Tversky and weighted BCE-Dice losses. These top-3 performing models are used to construct the ensemble. Here, the lung masks predicted by the top-3 performing models are bitwise-ANDed to produce the final lung mask. We observed that the IoU, Dice coefficient, and accuracy, achieved using the bitwise-ANDed model ensemble are superior compared to any individual constituent model. However, we observed no statistically significant difference in performance ($p > 0.05$) between the individual models and the ensemble.

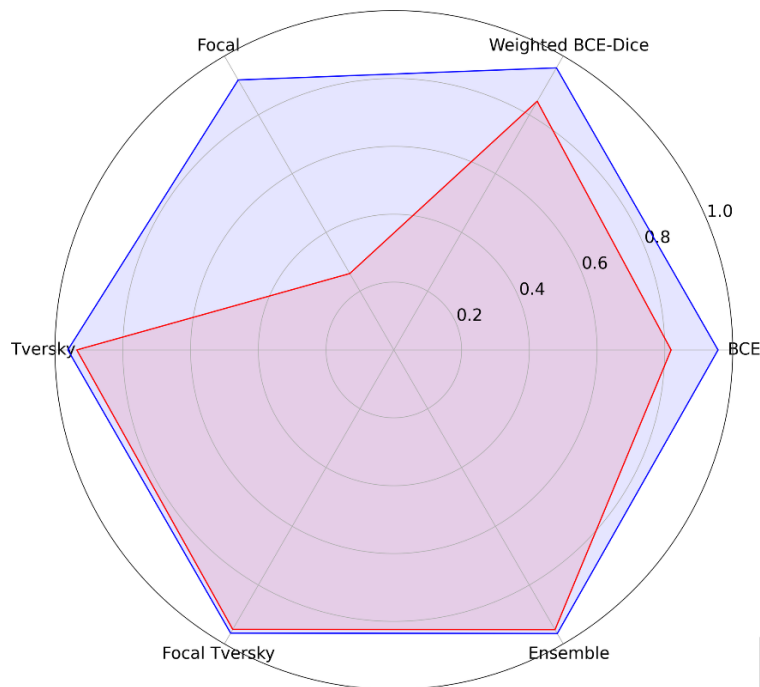


Fig 3. Polar coordinates plot showing IoU, and Dice coefficient values obtained with the segmentation model that is trained with the loss functions discussed in this study. In general, the model demonstrated higher values for the Dice coefficient compared to IoU.

We used the top-3 performing models and the bitwise-ANDed ensemble approach to predict lung masks for the CXRs in the pediatric pneumonia CXR collection. As the ground truth lung masks for these CXRs are not made available by the authors of [7], the segmentation performance could not be validated. The predicted lung masks are overlaid on the original CXRs to delineate the lung boundaries and are cropped. The cropped images are resized to 512×512 pixel resolution and used for further analysis (i.e., disease classification).

3.2. CXR disease classification

Recall that the encoder from the trained EfficientNet-B0-based U-Net model is truncated and appended with classification layers. This approach is followed to perform a CXR modality-specific knowledge

transfer to improve performance in a relevant task of classifying the CXRs in the pediatric pneumonia CXR collection into normal, bacterial pneumonia, or viral pneumonia categories. The classification models are trained to minimize the loss functions discussed in Section 2.3.1. Fig 4 and Table 2 summarizes the classification performance achieved by these models. We measured the 95% CI as the exact Clopper–Pearson interval for the MCC metric to test for statistical significance. It is observed from Fig 4 that the classification models demonstrated higher values for F-score compared to the MCC metric. F-score provides a balanced measure of precision and recall but could provide a biased estimate since it does not consider TN values. MCC considers TPs, TNs, FPs, and FNs in its computation. The score of MCC lies in the range $[-1, +1]$ where $+1$ demonstrates a perfect model while -1 demonstrates poor performance. The authors of [41] discuss the benefits of using MCC metric over F-score and accuracy in evaluating classification models. It is observed from Table 2 that the model trained to minimize the calibrated CCE loss demonstrated superior values for accuracy (0.9343), AUROC (0.9928), AUPRC (0.9869), precision (0.9345), recall (0.9343), F-score (0.9338), and MCC (0.8996) metrics. The 95% CI for the MCC metric demonstrated a tighter error margin and hence higher precision as compared to other models. The performance achieved with the calibrated CCE loss is significantly superior ($p < 0.05$) as compared to those achieved by the models that are trained to minimize the categorical focal and calibrated categorical focal loss functions. Fig 5 shows the confusion matrix, AUROC, and AUPRC curves obtained with the calibrated CCE loss-trained model. This performance is followed by the models that are trained to minimize the CCE with entropy-based regularization, calibrated negative entropy, calibrated CCE, smoothed-focal-0.2, smoothed-CCE-0.2, categorical-Hinge, categorical focal, calibrated focal, calibrated KL divergence, and calibrated Hinge loss functions.

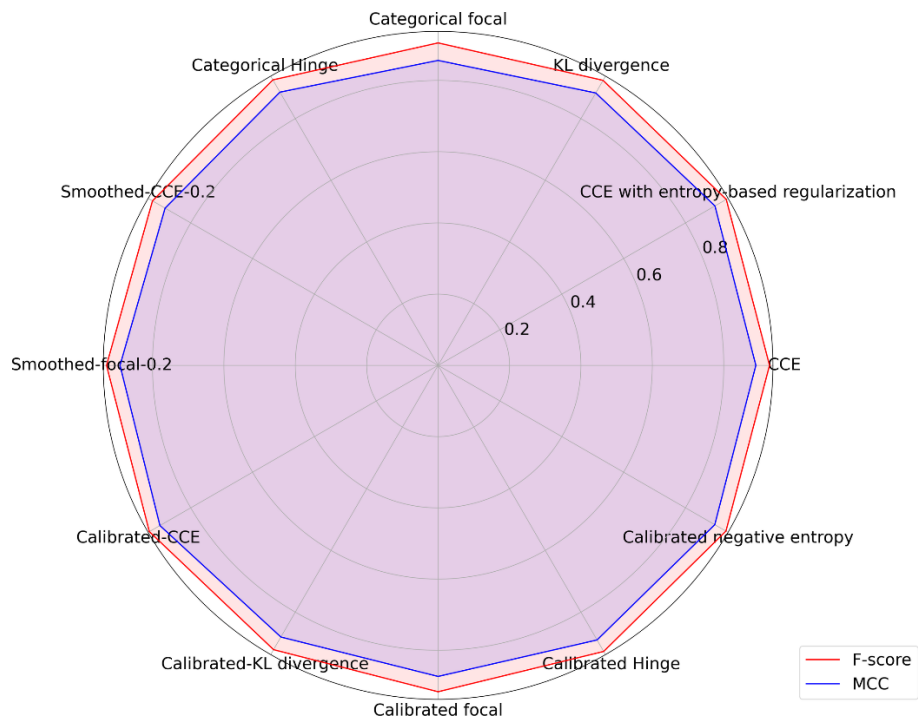


Fig 4. Polar coordinates plot showing the F-score and MCC values achieved by the classification models. The models demonstrated higher values for the F-score compared to MCC.

Table 2. Classification performance achieved by the classification models that are trained using the loss functions discussed in this study. The top-K (K = 3, 5) models are selected based on the MCC metric. The values in parentheses denote the 95% CI measured as the exact Clopper–Pearson interval for the MCC metric. Bold numerical values denote superior performance in respective columns.

Loss	Metrics						
	Accuracy	AUROC	AUPRC	Precision	Recall	F-Score	MCC
CCE	0.9279	0.9921	0.9857	0.9292	0.9279	0.9282	0.8899 (0.8653, 0.9145)
CCE with entropy-based regularization ($\beta=2.0$)	0.9311	0.9913	0.9844	0.9337	0.9311	0.9319	0.8953 (0.8712, 0.9194)
KL divergence	0.9231	0.99	0.9825	0.9261	0.9231	0.924	0.8831 (0.8578, 0.9084)
Categorical focal ($\gamma = 1$)	0.9054	0.984	0.9753	0.9079	0.9054	0.9054	0.8562 (0.8286, 0.8838)
Categorical Hinge	0.9247	0.9892	0.9803	0.928	0.9247	0.9255	0.8858 (0.8608, 0.9108)
Smoothed-CCE ($\sigma = 0.2$)	0.9231	0.9899	0.9821	0.9252	0.9231	0.9237	0.8829 (0.8576, 0.9082)
Smoothed-focal ($\sigma = 0.2$)	0.9279	0.9847	0.9744	0.9317	0.9279	0.9287	0.8909 (0.8664, 0.9154)
Calibrated-CCE ($\lambda = 10$)	0.9343	0.9928	0.9869	0.9345	0.9343	0.9338	0.8996 (0.876, 0.9132)
Calibrated-KL divergence ($\lambda = 1$)	0.9215	0.9895	0.9817	0.9239	0.9215	0.9217	0.8807 (0.8552, 0.9062)
Calibrated focal ($\gamma = \lambda = 1$)	0.9167	0.986	0.9777	0.9187	0.9167	0.9164	0.8734 (0.8473, 0.8995)

Calibrated Hinge ($\lambda = 10$)	0.9279	0.9894	0.9803	0.9292	0.9279	0.9275	0.8903 (0.8657, 0.9149)
Calibrated negative entropy($\beta = 1e-3$; $\lambda = 10$)	0.9311	0.9917	0.9851	0.9316	0.9311	0.9308	0.8947 (0.8706, 0.9188)

The top-3 (i.e., models that are trained to minimize the calibrated CCE, CCE with entropy-based regularization, and calibrated negative entropy losses) and top-5 (i.e., models that are trained to minimize the calibrated CCE, CCE with entropy-based regularization, calibrated negative entropy, label-smoothed categorical focal, and calibrated categorical Hinge losses) are used to construct prediction-level and model-level ensembles. Recall that for the prediction-level ensemble, the models' predictions are combined using majority voting, simple averaging, weighted averaging, and stacking-based ensemble methods. Fig 6 and Table 3 summarizes the classification performance achieved by the prediction-level ensembles.

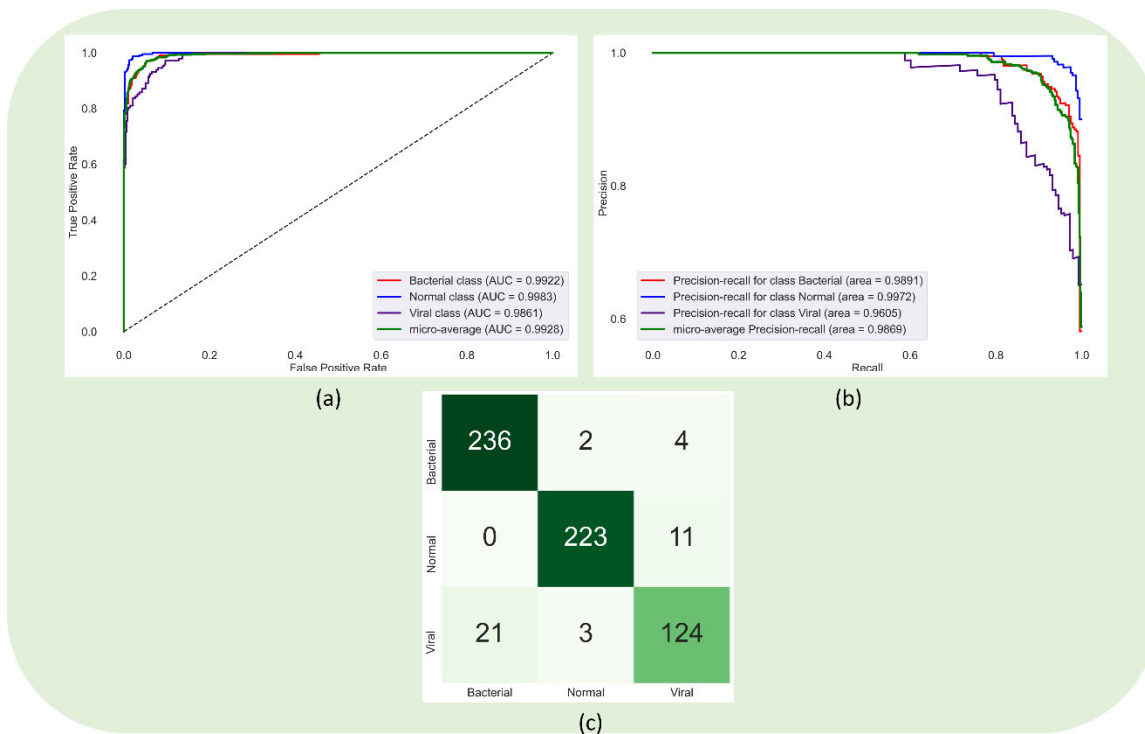


Fig 5. Confusion matrix, AUROC, and AUPRC curves obtained using the model that is trained to minimize the calibrated CCE loss function.

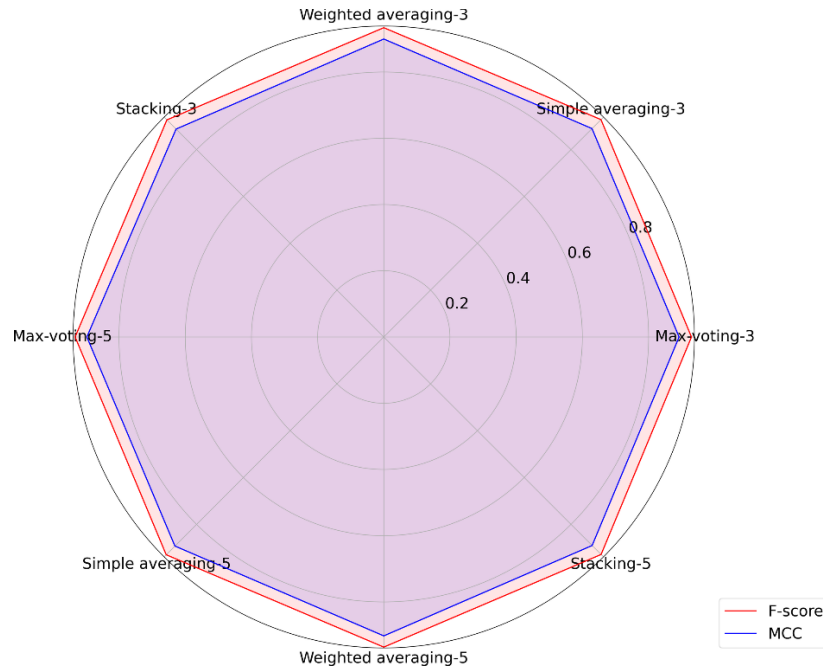


Fig 6. polar coordinates plot showing the F-score and MCC values achieved by the prediction-level ensembles. The ensemble demonstrated higher values for the F-score compared to the MCC metric.

It is observed from Fig 6 that the prediction-level ensembles constructed using the top-3 and top-5 performing models demonstrated higher values for F-score as compared to the MCC metrics for the reasons discussed before.

Table 3. Performance metrics achieved by the prediction-level ensembles using the top-K (K=3, 5) models. The values in parentheses denote the 95% CI measured as the exact Clopper–Pearson interval for the MCC metric. Bold numerical values denote superior performance in respective columns.

Models	Method	Metrics						
		Accuracy	AUROC	AUPRC	Precision	Recall	F-Score	MCC
Top-3	Max voting	0.9295	0.9471	0.9412	0.9305	0.9295	0.9297	0.8923 (0.8679, 0.9167)
	Simple averaging	0.9279	0.9924	0.9863	0.9287	0.9279	0.9281	0.8898 (0.8652, 0.9144)
	Weighted averaging	0.9343	0.9925	0.9865	0.9345	0.9343	0.9338	0.8996 (0.876, 0.9232)
	Stacking	0.9263	0.99	0.9831	0.9284	0.9263	0.9269	0.8877 (0.8629, 0.9125)
Top-5	Max voting	0.9327	0.9495	0.9439	0.9334	0.9327	0.9327	0.8972 (0.8733, 0.9211)
	Simple averaging	0.9295	0.9923	0.9863	0.9311	0.9295	0.9298	0.8926

								(0.8683, 0.9169)
	Weighted averaging	0.9359	0.9925	0.9865	0.9375	0.9359	0.9363	0.9024 (0.8791, 0.9157)
	Stacking	0.9279	0.9873	0.9801	0.9303	0.9279	0.9286	0.8903 (0.8657, 0.9149)

It is observed from Table 3 that the weighted averaging ensemble of the top-5 performing models using the optimal weights [0.40560531, 0.192276399, 0.00356809023, 0.3985502, 1.10927275e-16] calculated using the SLSQP method achieved superior performance compared to other ensembles. The 95% CI obtained using the MCC metric demonstrated a tighter error margin and hence higher precision compared to other ensemble methods. However, we observed no statistically significant difference ($p > 0.05$) in performance across the ensemble methods. Fig 7 shows the confusion matrix, AUROC, and AUPRC curves achieved using the top-5 weighted averaging ensemble. Recall that the model-level ensembles are constructed using the top-K ($K=3, 5$) models by instantiating them with their trained weights and truncating them at their deepest convolutional layers. The feature maps from these layers are concatenated and appended with a 1×1 convolutional layer for feature dimensionality reduction. In our study, the feature maps of the deepest convolutional layers for the models have [16, 16, 512] dimensions. Hence, after concatenation, the feature maps for the top-3 models are of [16, 16, 1536] dimensions, and that for the top-5 models are of [16, 16, 2560] dimensions. We used 1×1 convolutions to reduce these dimensions to [16, 16, 512]. The 1×1 convolutional layer is appended with a GAP and dense layer with three neurons to classify the CXRs into normal, bacterial pneumonia, or viral pneumonia categories. Table 4 shows the classification performance achieved in this regard. We observed no statistically significant difference ($p > 0.05$) in performance between the top-3 and top-5 model-level ensembles. We further performed a weighted averaging of the predictions of the top-3 and top-5 model-level ensembles. We calculated the optimal weights [0.3764, 0.6236] using the SLSQP method to improve performance. Fig 8 shows the confusion matrix, AUROC, and AUPRC curves obtained by the weighted averaging ensemble using the predictions of the top-3 and top-5 model-level ensembles. We observed that this ensemble approach demonstrated superior performance for all metrics compared to the individual models and all ensemble methods discussed in this study.

Table 4. Classification performance achieved by model-level ensembles. The values in parentheses denote the 95% CI measured as the exact Clopper–Pearson interval for the MCC metric.

Method	Metrics						
	Accuracy	AUROC	AUPRC	Precision	Recall	F-Score	MCC
Top-3	0.9327	0.9933	0.9881	0.9334	0.9327	0.933	0.897

							(0.8731, 0.9209)
Top-5	0.9359	0.9928	0.9872	0.9365	0.9359	0.936	0.9019 (0.8785, 0.9253)
Weighted averaging	0.9391	0.9933	0.9881	0.9396	0.9391	0.9392	0.9068 (0.8839, 0.9297)

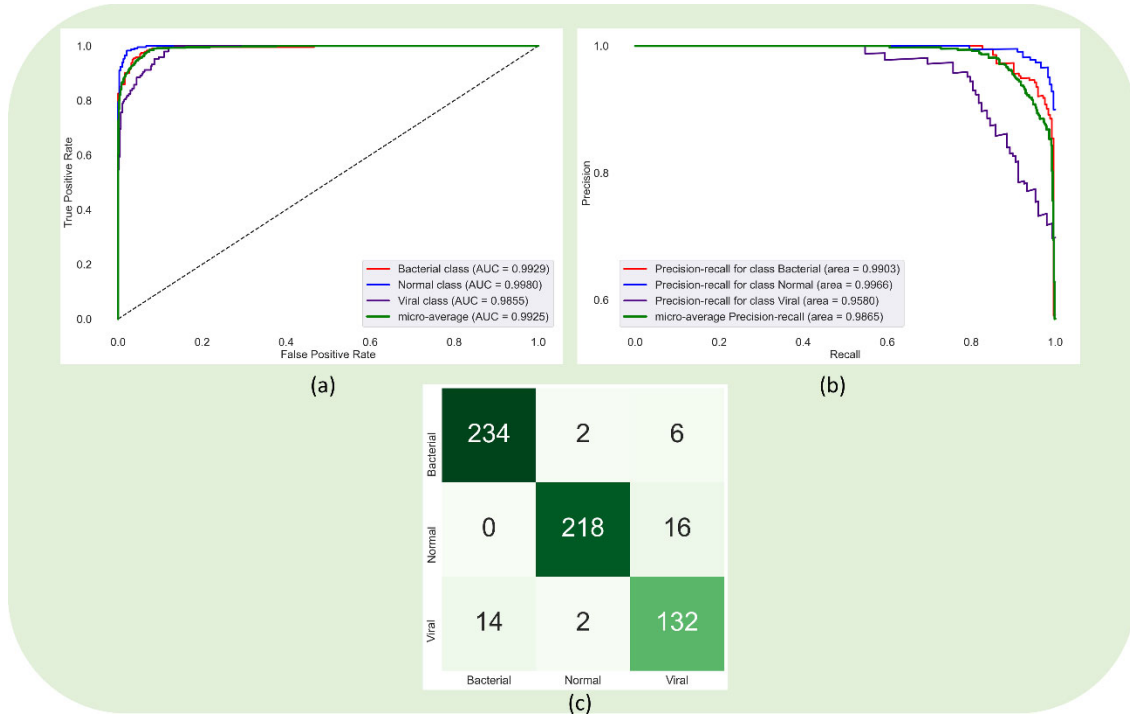


Fig 7. Confusion matrix, AUROC, and AUPRC curves obtained by the weighted averaging ensemble of the top-5 performing models.

Table 5 shows a comparison of the performance achieved with (i) the weighted averaging ensemble of top-3 and top-5 model-level predictions and (ii) SOTA literature.

Table 5. Comparison of the proposed approach with the SOTA literature. The values in parentheses denote the 95% CI measured as the exact Clopper–Pearson interval for the MCC metric.

Study	Metrics						
	Acc.	AUROC	AUPRC	Prec.	Rec.	F	MCC
Kermany et al. [7]	NA	NA	NA	NA	NA	NA	NA
Rajaraman et al. [33]	0.918	0.939	NA	0.92	0.9	0.91	0.87 (0.8436, 0.8964)
Proposed	0.9391	0.9933	0.9881	0.9396	0.9391	0.9392	0.9068 (0.8839, 0.9297)

The authors of [7] that released the pediatric pneumonia CXR dataset performed binary classification to classify the CXRs as showing normal lungs or other abnormal manifestations. To the best of our knowledge, only the authors of [33] performed a multi-class classification using the train and test splits released by the authors of [7]. We observed that the MCC metric achieved by the weighted averaging ensemble of top-3 and top-5 model-level predictions is significantly superior ($p < 0.05$) compared to the MCC metric reported in the literature [33].

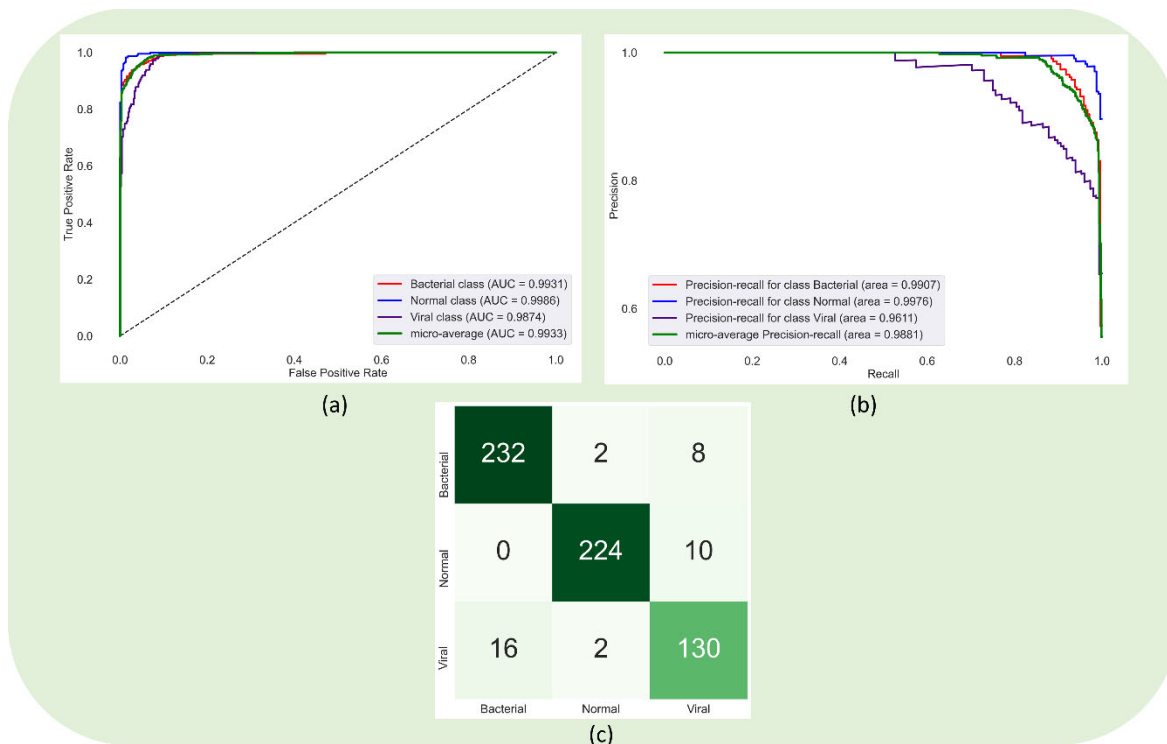


Fig 8. Confusion matrix, AUROC, and AUPRC curves obtained through the weighted averaging ensemble of the predictions of top-3 and top-5 model level ensembles.

3.3. Disease ROI localization

We used Grad-CAM visualization tools for localizing the disease-manifested ROIs to ensure that the models learned meaningful features. Fig 9 shows instances of pediatric CXRs showing expert ground truth annotations for bacterial and viral pneumonia manifestations and Grad-CAM localizations of the top-5 performing models and the top-5 model-level ensemble. It is observed from Fig 9 that the classification models trained using the existing and proposed loss functions and the top-5 model-level ensemble highlighted the ROIs showing disease manifestations. The highest activations, observed as the hottest region in the heatmap, contribute the majority toward the models' decision toward classifying the CXRs into their respective categories.

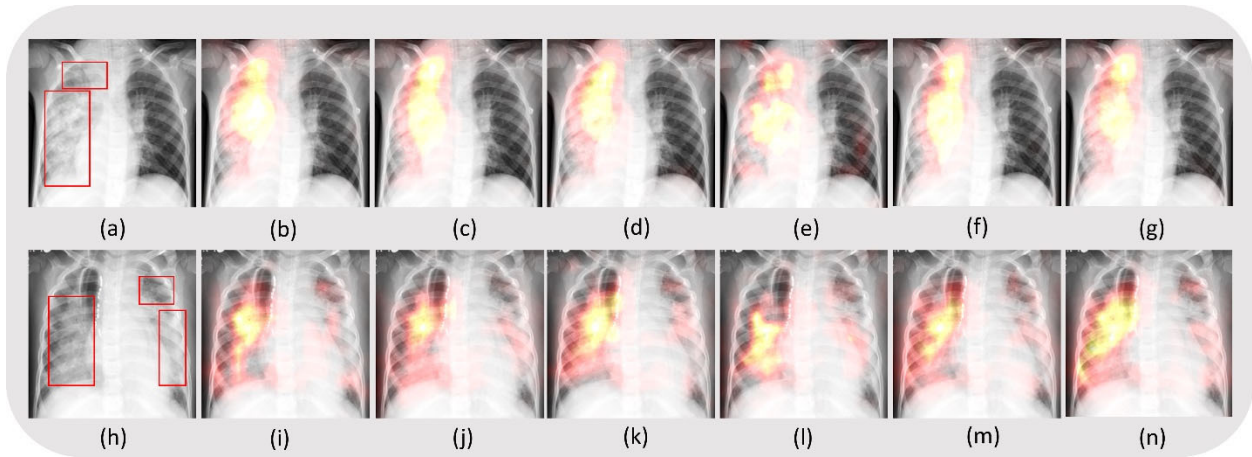


Fig 9. Grad-CAM-based localization of the disease ROIs. (a) and (h) denote instances of CXR with expert annotations showing bacterial and viral pneumonia manifestations, respectively. The sub-parts (b), (c), (d), (e), (f), and (g) show Grad-CAM-based ROI localization achieved using the models trained with calibrated CCE, CCE with entropy-based regularization, calibrated negative entropy, label-smoothed categorical focal, calibrated categorical Hinge loss functions, and the top-5 model-level ensemble, respectively, highlighting regions of bacterial pneumonia manifestations. The sub-parts (i), (j), (k), (l), (m), and (n) show the localization achieved using the models in the same order as above, highlighting viral pneumonia manifestations.

4. Discussion and conclusion

While several studies [42 – 46] report using the pediatric pneumonia CXR dataset [7] in a binary classification setting, only the authors of [33] trained models for a multi-class classification task. Further, studies in [42 – 46] used ImageNet-pretrained models to transfer knowledge to a target CXR classification task as opposed to a CXR modality-specific pretrained model. Such transfer of knowledge may not be relevant since the characteristics of natural images are distinct from medical images. In this work, we propose to resolve the aforementioned issues by transferring knowledge from a CXR modality-specific pretrained model to improve performance in a relevant CXR classification task. We trained the models using existing loss functions and also proposed several loss functions. Our experimental results showed that the model trained to minimize the calibrated CCE loss demonstrated superior values for all metrics. This performance is followed by those that are trained to minimize the proposed losses such as CCE with entropy-based regularization, calibrated negative entropy, label-smoothed categorical focal, and calibrated categorical Hinge loss.

We evaluated the performance of both prediction-level and model-level ensembles. We observed from the experiments that the model-level ensembles demonstrated markedly improved performance than the prediction-level ensembles. We further improved performance by (i) deriving optimal weights using the SLSQP method, and (ii) using the derived weights to perform weighted averaging of the predictions of top-

3 and top-5 model-level ensembles. We observed that the weighted averaging ensemble demonstrated superior performance for all metrics compared to other individual models, their ensemble, and the SOTA literature. Finally, we used Grad-CAM-based visualization tools to interpret the learned weights in the individual models and model-level ensembles. We observed that these models precisely localized the ROIs showing disease manifestations, confirming the expert's knowledge of the problem.

Our study combined the benefits of (i) performing CXR modality-specific knowledge transfer, (ii) proposing loss functions that delivered superior classification performance in a multi-class classification setting, (iii) constructing prediction-level and model-level ensembles to achieve SOTA performance as shown in Table 5. However, there are a few limitations to this study. For instance, we used an EfficientNet-B0 based U-Net model to segment the lungs and used the model further to perform CXR modality-specific knowledge transfer. Future research could focus on transferring knowledge using other models or a model ensemble that are trained in a supervised, semi-supervised, or unsupervised setting. Novel loss functions could be proposed for classification tasks to train models and their ensembles. Other ensemble methods such as blending and snapshots [47] could also be attempted to improve performance. It is becoming increasingly viable to deploy ensemble models in real-time with the advent of low-cost computation, storage solutions, and cloud technology. The methods proposed in this study could be extended to the classification and detection of cardiopulmonary abnormalities including COVID-19, TB, cardiomegaly, and lung nodules, among others.

Acknowledgment

This study is supported by the Intramural Research Program (IRP) of the National Library of Medicine (NLM) and the National Institutes of Health (NIH).

References

1. Chan HP, Samala RK, Hadjiiski LM, Zhou C. Deep Learning in Medical Image Analysis. *Adv Exp Med Biol.* 2020;1213:3-21. doi: 10.1007/978-3-030-33128-3_1. PMID: 32030660; PMCID: PMC7442218.
2. Rajpurkar P, Irvin J, Ball RL, Zhu K, Yang B, Mehta H, Duan T, Ding D, Bagul A, Langlotz CP, Patel BN, Yeom KW, Shpanskaya K, Blankenberg FG, Seekins J, Amrhein TJ, Mong DA, Halabi SS, Zucker EJ, Ng AY, Lungren MP. Deep learning for chest radiograph diagnosis: A retrospective comparison of the CheXNeXt algorithm to practicing radiologists. *PLoS Med.* 2018 Nov

- 20;15(11):e1002686. doi: 10.1371/journal.pmed.1002686. PMID: 30457988; PMCID: PMC6245676.
3. Rajaraman S, Sornapudi S, Alderson PO, Folio LR, Antani SK. Analyzing inter-reader variability affecting deep ensemble learning for COVID-19 detection in chest radiographs. *PLoS One*. 2020 Nov 12;15(11):e0242301. doi: 10.1371/journal.pone.0242301. PMID: 33180877; PMCID: PMC7660555.
 4. Wang X, Peng Y, Lu L, Lu Z, Bagheri M, Summers RM. ChestX-Ray8: Hospital-Scale Chest X-Ray Database and Benchmarks on Weakly-Supervised Classification and Localization of Common Thorax Diseases. *CVPR 2017*: 3462-3471
 5. Shih G, Wu CC, Halabi SS, Kohli MD, Prevedello LM, Cook TS, Sharma A, Amorosa JK, Arteaga V, Galperin-Aizenberg M, Gill RR, Godoy MCB, Hobbs S, Jeudy J, Laroia A, Shah PN, Vummididi D, Yaddanapudi K, Stein A. Augmenting the National Institutes of Health Chest Radiograph Dataset with Expert Annotations of Possible Pneumonia. *Radiol Artif Intell*. 2019 Jan 30;1(1):e180041. doi: 10.1148/ryai.2019180041. PMID: 33937785; PMCID: PMC8017407.
 6. Irvin J, Rajpurkar P, Ko M, et al. CheXpert: A Large Chest Radiograph Dataset with Uncertainty Labels and Expert Comparison. *AAAI 2019*: 590-597
 7. Kermany DS, Goldbaum M, Cai W, et al. Identifying Medical Diagnoses and Treatable Diseases by Image-Based Deep Learning. *Cell*. 2018 Feb 22;172(5):1122-1131.e9. doi: 10.1016/j.cell.2018.02.010. PMID: 29474911.
 8. Lakhani P, Sundaram B. Deep Learning at Chest Radiography: Automated Classification of Pulmonary Tuberculosis by Using Convolutional Neural Networks. *Radiology*. 2017 Aug;284(2):574-582. doi: 10.1148/radiol.2017162326. Epub 2017 Apr 24. PMID: 28436741.
 9. Lin TY, Goyal P, Girshick R, He K, Dollar P. Focal Loss for Dense Object Detection. *IEEE Trans Pattern Anal Mach Intell*. 2020 Feb;42(2):318-327. doi: 10.1109/TPAMI.2018.2858826. Epub 2018 Jul 23. PMID: 30040631.
 10. Tran GS, Nghiem TP, Nguyen VT, Luong CM, Burie JC. Improving Accuracy of Lung Nodule Classification Using Deep Learning with Focal Loss. *J Healthc Eng*. 2019;2019:5156416. Published 2019 Feb 4. doi:10.1155/2019/5156416
 11. Qiao Z, Bae A, Glass LM, Xiao C, Sun J. FLANNEL (Focal Loss bAsed Neural Network EnsemblE) for COVID-19 detection, *Journal of the American Medical Informatics Association*, Volume 28, Issue 3, March 2021, Pages 444–452, <https://doi.org/10.1093/jamia/ocaa280>
 12. Krizhevsky A, Sutskever I, Hinton GE. ImageNet Classification with Deep Convolutional Neural Networks. *NIPS 2012*: 1106-1114

13. Yadav O, Passi K, Jain CK. Using Deep Learning to Classify X-ray Images of Potential Tuberculosis Patients. In 2018 IEEE International Conference on Bioinformatics and Biomedicine (BIBM), 2018, pp. 2368-2375, doi: 10.1109/BIBM.2018.8621525.
14. Rajaraman S, Siegelman J, Alderson PO, Folio LS, Folio LR, Antani SK. Iteratively Pruned Deep Learning Ensembles for COVID-19 Detection in Chest X-rays. IEEE Access. 2020;8:115041-115050. doi: 10.1109/access.2020.3003810. Epub 2020 Jun 19. PMID: 32742893; PMCID: PMC7394290.
15. Rajaraman S, Kim I, Antani SK. Detection and visualization of abnormality in chest radiographs using modality-specific convolutional neural network ensembles. PeerJ. 2020 Mar 17;8:e8693. doi: 10.7717/peerj.8693. PMID: 32211231; PMCID: PMC7083159.
16. Rajaraman S, Antani SK. Modality-specific deep learning model ensembles toward improving TB detection in chest radiographs. IEEE Access. 2020;8:27318-27326. doi: 10.1109/access.2020.2971257. Epub 2020 Feb 3. PMID: 32257736; PMCID: PMC7120763.
17. Demner-Fushman D, Kohli MD, Rosenman MB, et al. Preparing a collection of radiology examinations for distribution and retrieval. J Am Med Inform Assoc. 2016;23(2):304-310. doi:10.1093/jamia/ocv080
18. Zamzmi G, Rajaraman S, Antani S. UMS-Rep: Unified modality-specific representation for efficient medical image analysis. Informatics in Medicine Unlocked. Volume 24, 2021, 100571, ISSN 2352-9148, <https://doi.org/10.1016/j.imu.2021.100571>.
19. Hosni M, Carrillo-de-Gea JM, Idri A, Fernandez-Aleman JL, Garcia-Berna JA. Using ensemble classification methods in lung cancer disease. Annu Int Conf IEEE Eng Med Biol Soc. 2019 Jul;2019:1367-1370. doi: 10.1109/EMBC.2019.8857435. PMID: 31946147.
20. Islam MT, Aowal MA, Minhaz AT, Ashraf K. Abnormality Detection and Localization in Chest X-Rays using Deep Convolutional Neural Networks. CoRR abs/1705.09850 (2017)
21. Zhou T, Lu H, Yang Z, Qiu S, Huo B, Dong Y. The ensemble deep learning model for novel COVID-19 on CT images. Appl Soft Comput. 2021;98:106885. doi:10.1016/j.asoc.2020.106885
22. AlJame M, Ahmad I, Imtiaz A, Mohammed A. Ensemble learning model for diagnosing COVID-19 from routine blood tests. Informatics in Medicine Unlocked, volume 21, 2020, 100449, ISSN 2352-9148, <https://doi.org/10.1016/j.imu.2020.100449>.
23. Mohammed EA, Keyhani M, Sanati-Nezhad A. et al. An ensemble learning approach to digital corona virus preliminary screening from cough sounds. Sci Rep 11, 15404 (2021). <https://doi.org/10.1038/s41598-021-95042-2>

24. Chowdhury NK, Kabir MA, Rahman MM, Rezoana N. ECOVNet: a highly effective ensemble based deep learning model for detecting COVID-19. *PeerJ Comput Sci.* 2021 May 26;7:e551. doi: 10.7717/peerj-cs.551. PMID: 34141883; PMCID: PMC8176542.
25. Candemir S, Jaeger S, Palaniappan K, Musco JP, Singh RK, Zhiyun Xue, Karargyris A, Antani S, Thoma G, McDonald CJ. Lung segmentation in chest radiographs using anatomical atlases with nonrigid registration. *IEEE Trans Med Imaging.* 2014 Feb;33(2):577-90. doi: 10.1109/TMI.2013.2290491. Epub 2013 Nov 13. PMID: 24239990.
26. Tan M, Le QV. EfficientNet: Rethinking Model Scaling for Convolutional Neural Networks. *ICML* 2019: 6105-6114.
27. Jaeger S, Candemir S, Antani S, Wang YX, Lu PX, Thoma G. Two public chest X-ray datasets for computer-aided screening of pulmonary diseases. *Quant Imaging Med Surg.* 2014;4(6):475-477. doi:10.3978/j.issn.2223-4292.2014.11.20
28. Ronneberger O, Fischer P, Brox T. U-Net: Convolutional Networks for Biomedical Image Segmentation. *MICCAI* (3) 2015: 234-241
29. Yakubovskiy P. Segmentation Models. 2019, GitHub repository. Available at: https://github.com/qubvel/segmentation_models
30. Reamaroon N, Sjoding MW, Derksen, H. et al. Robust segmentation of lung in chest x-ray: applications in analysis of acute respiratory distress syndrome. *BMC Med Imaging* 20, 116 (2020). <https://doi.org/10.1186/s12880-020-00514-y>
31. Salehi SSM, Erdogmus D, Gholipour A. Tversky Loss Function for Image Segmentation Using 3D Fully Convolutional Deep Networks. *MLMI@MICCAI 2017*: 379-387
32. Abraham N, Khan NM. A Novel Focal Tversky Loss Function With Improved Attention U-Net for Lesion Segmentation. *ISBI 2019*: 683-687
33. Rajaraman S, Candemir S, Kim I, Thoma G, Antani S. Visualization and Interpretation of Convolutional Neural Network Predictions in Detecting Pneumonia in Pediatric Chest Radiographs. *Applied Sciences.* 2018; 8(10):1715. <https://doi.org/10.3390/app8101715>
34. Zahery M, Maes HH, Neale MC. CSOLNP: Numerical Optimization Engine for Solving Non-linearly Constrained Problems. *Twin Res Hum Genet.* 2017;20(4):290–297. pmid:28535831
35. Liang G, Zhang Y, Wang X, Jacobs N. Improved Trainable Calibration Method for Neural Networks on Medical Imaging Classification. *CoRR abs/2009.04057* (2020)
36. Razzak I, Blumenstein M, Xu G. Multiclass Support Matrix Machines by Maximizing the Inter-Class Margin for Single Trial EEG Classification. *IEEE Trans Neural Syst Rehabil Eng.* 2019 Jun;27(6):1117-1127. doi: 10.1109/TNSRE.2019.2913142. Epub 2019 Apr 25. PMID: 31021801.

37. Zhang CB, Jiang PT, Hou Q, Wei Y, Han Q, Li Z, Cheng MM. Delving Deep Into Label Smoothing. *IEEE Trans Image Process.* 2021;30:5984-5996. doi: 10.1109/TIP.2021.3089942. Epub 2021 Jun 30. PMID: 34166191.
38. Guo C, Pleiss G, Sun Y, Weinberger KQ. On the calibration of modern neural networks. In *Proc. ICML*, pages 1321–1330, 2017.
39. Zhou B, Khosla A, Lapedriza A, Oliva A, Torralba A. Learning Deep Features for Discriminative Localization. *CVPR 2016*: 2921-2929
40. Selvaraju RR, Cogswell M, Das A, Vedantam R, Parikh D, Batra D. Grad-CAM: Visual Explanations from Deep Networks via Gradient-Based Localization. In *2017 IEEE International Conference on Computer Vision (ICCV)*, 2017, pp. 618-626, doi: 10.1109/ICCV.2017.74.
41. Chicco D, Jurman G. The advantages of the Matthews correlation coefficient (MCC) over F1 score and accuracy in binary classification evaluation. *BMC Genomics* 21, 6 (2020). <https://doi.org/10.1186/s12864-019-6413-7>
42. Ferreira JR, Cardenas DAC, Moreno RA, de Fátima de Sá Rebelo M, Krieger JE, Gutierrez MA. Multi-View Ensemble Convolutional Neural Network to Improve Classification of Pneumonia in Low Contrast Chest X-Ray Images. In *2020 42nd Annual International Conference of the IEEE Engineering in Medicine & Biology Society (EMBC)*, 2020, pp. 1238-1241, doi: 10.1109/EMBC44109.2020.9176517.
43. Tang YX, Tang YB, Peng Y. et al. Automated abnormality classification of chest radiographs using deep convolutional neural networks. *npj Digit. Med.* 3, 70 (2020). <https://doi.org/10.1038/s41746-020-0273-z>
44. Saraiva A, Ferreira N, Lopes de Sousa L, Costa N, Sousa J, Santos D, Valente A, Soares S. Classification of Images of Childhood Pneumonia using Convolutional Neural Networks. In *Proceedings of the 12th International Joint Conference on Biomedical Engineering Systems and Technologies - Volume 2: BIOIMAGING*, ISBN 978-989-758-353-7, pages 112-119, 2019. DOI: 10.5220/0007404301120119
45. Liz H, Sánchez-Montañés M, Tagarro A, Domínguez-Rodríguez S, Dagan R, Camacho D. Ensembles of Convolutional Neural Network models for pediatric pneumonia diagnosis. *Future Generation Computer Systems.* Volume 122, 2021, Pages 220-233, ISSN 0167-739X, <https://doi.org/10.1016/j.future.2021.04.007>.
46. E L, Zhao B, Guo Y, Zheng C, Zhang M, Lin J, Luo Y, Cai Y, Song X, Liang H. Using deep-learning techniques for pulmonary-thoracic segmentations and improvement of pneumonia diagnosis in pediatric chest radiographs. *Pediatr Pulmonol.* 2019 Oct;54(10):1617-1626. doi: 10.1002/ppul.24431. Epub 2019 Jul 3. PMID: 31270968.

47. P, SAB, Annavarapu CSR. Deep learning-based improved snapshot ensemble technique for COVID-19 chest X-ray classification. *Appl Intell* 51, 3104–3120 (2021). <https://doi.org/10.1007/s10489-021-02199-4>